J Mater Sci

Metals & corrosion

Size and shape effects on the strength of platinum nanoparticles

J. Zimmerman[1], A. Bisht[1], Y. Mishin[2], and E. Rabkin[1],*

[1] *Department of Material Science and Engineering, Technion–Israel Institute of Technology, 3200003 Haifa, Israel*
[2] *Department of Physics and Astronomy, George Mason University, MSN 3F3, Fairfax, VA 22030, USA*

Received: 6 April 2021
Accepted: 8 August 2021

ABSTRACT

Several previous studies demonstrated that defect-free faceted nanocrystals of face-centered cubic metals (such as Au, Ni, and Pd) exhibit extraordinarily high mechanical strength approaching the theoretical strength of the respective metals. In the present work, we have studied the compressive strength of Pt nanoparticles fabricated by the solid-state dewetting method optimized for producing nanoparticles with a variety of shapes and sizes. The particles exhibit a well-pronounced size effect on strength, with the smallest particles achieving the highest compressive strength of 9.5 GPa corresponding to the lower limit of the theoretical strength of Pt. However, the average strength of the Pt particles normalized by the respective shear modulus is significantly lower than that of Au and Ni nanoparticles fabricated by a similar dewetting method. We have also established a correlation between the particles strength and shape described by the ratio of the particle top facet and projected diameters. Smaller values of this ratio correlate with higher compressive strength. Based on the experimental data obtained, we formulate a power law describing the combined effect of the particle size and shape on its strength. Our results are in qualitative agreement with previous computational studies demonstrating that the theoretical strength of Pt normalized by its shear modulus is significantly lower than that of other face-centered cubic metals.

Handling Editor: N. Ravishankar.

Address correspondence to E-mail: Erabkin@technion.ac.il

https://doi.org/10.1007/s10853-021-06435-7

Springer

GRAPHICAL ABSTRACT

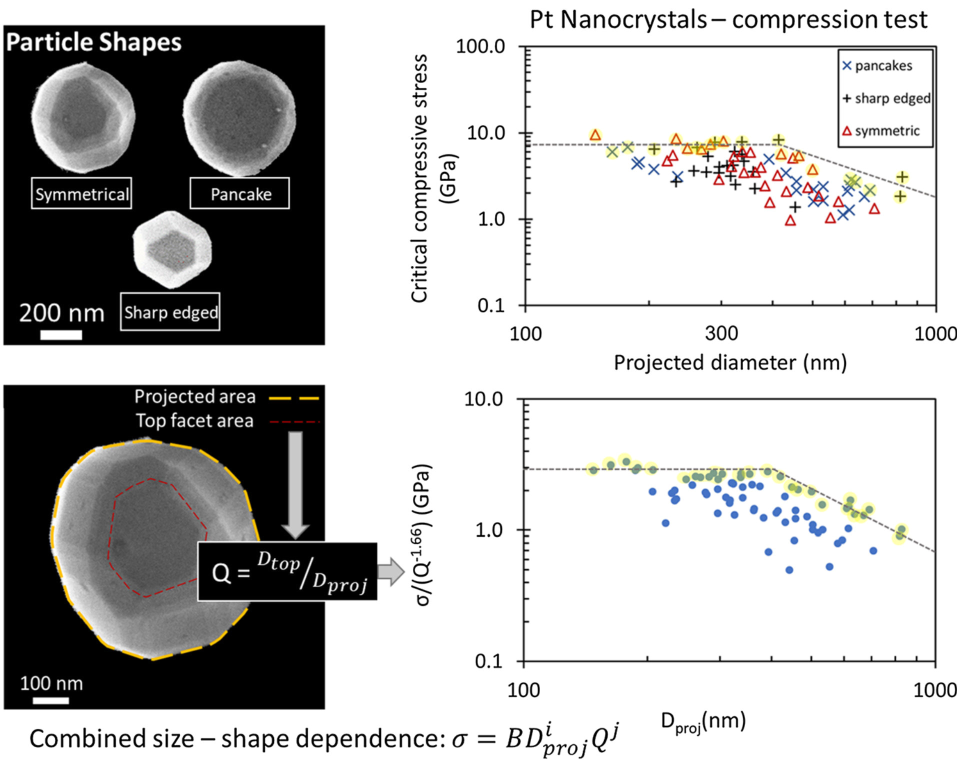

Introduction

Nanoparticles of noble metals find a wide range of applications in sensing [1, 2], theranostics [3], opto-electronics [4], catalysis [5], and in micro-electromechanical systems (MEMS) [6]. A large variety of currently available processing methods enable the fabrication of metal nanoparticles of different shapes and sizes [7, 8]. A better understanding of the size and shape effects on the properties of nanoparticles would enable their more efficient use and open new application areas.

Mechanical properties of metal nanoparticles have recently received much attention due to their relevance to applications in tribology (e.g., additives to lubricants), polishing and finishing (e.g., abrasive additives in chemical mechanical polishing applications) [9], and most notably, energy storage and conversion [10, 11]. Also, strain engineering of metal nanoparticles is an emerging new method of improving their catalytic performance [12, 13]. Metal nanoparticles also represent convenient objects for testing the fundamental aspects of materials behavior at ultra-high stresses since they easily fit in the confined environment of the diamond anvil cell [14] and can be easily produced in a defect-free state enabling elastic deformation up to several percent [15]. Mechanical properties of noble metal nanoparticles are especially interesting since the disturbing effect of the native oxide film on the nanoparticle behavior can be avoided [16]. Furthermore, the maximum tensile stress that the nanoparticle can sustain before the onset of plastic yielding determines the energy barrier for the Kirkendall hollowing of the core–shell nanoparticles [17].

The deformation mechanisms of metal nanoparticles are remarkably different from those in the bulk material. In bulk metals, the onset of plastic deformation is associated with the motion of pre-existing dislocations on energetically favored slip planes and/or the activation of available dislocation sources [18]. In a pristine nanoparticle, no such dislocations exist, making the nucleation of new dislocations the critical step of plastic deformation [19, 20]. Two classical models describe the upper limit of the pristine particle strength. The Polanyi and Frenkel model estimates the upper limit of the material's shear strength as $G/2\pi$, whereas the more elaborate approach by Mackenzie [21] estimates the ultimate shear strength by $G/30$, where G is the shear modulus in the active slip system. Both models predict the shear strength to be orders of magnitude higher than the experimentally measured strength of bulk materials. Also, since the models mentioned above consider a homogeneous sliding of two crystal halves past each other, the calculated strength does not depend on the specimen's size. Bridging the gap between the theoretical and experimental strength motivated the active research on mechanics of pristine nanomaterials for more than three decades.

The focus of nanomechanical studies of sub-micrometer-sized metal samples was primarily on the absolute value of the strength and its size effect. Early studies on microwhiskers [22] and later on focused ion beam (FIB)-milled pillars [20, 23, 24] demonstrated strength values a factor of 3–50 higher than the strength of the respective bulk material, with a pronounced size effect ("smaller is stronger"). More recently, several studies have demonstrated that the theoretical strength limit can be achieved in pristine metal samples of sub-micrometer dimensions, such as Mo pillars [25], Pd nanowhiskers [26], Ni_3Al and Ag nanocubes [27, 28], and Fe, Au, and Ni nanoparticles [29–31], with the former five reporting a weak or non-existent size effect. It was also found that the equilibrated nanoparticles fabricated by solid-state dewetting are stronger than pristine nanopillars of similar size made of the same material. Mordehai et al. [32] linked the size dependence of the strength of faceted nanoparticles with stress concentration within the particle. In contrast, other authors link the size effect with a higher probability of finding dislocations and their sources in larger samples, especially in the case of FIB-milled nanopillars [30, 33]. We reiterate that the mechanisms controlling the strength are different in defect-free nanoparticles than in nanopillars or nanowhiskers.

The effect of elastic strain on the catalytic activity of Pt nanoparticles is the subject of intensive ongoing studies [34, 35]. For example, it was shown that a compressive strain of about 5% induced by a substrate causes a 90% increase in the catalytic activity of Pt nanoparticles in the oxygen reduction reaction [34]. Therefore, determining the maximum stress that Pt nanoparticles can sustain without plastic deformation is of high interest. To the best of our knowledge, no systematic studies of the mechanical properties of Pt nanoparticles were reported in the literature. To fill this gap of knowledge, we perform here nanomechanical compression testing of Pt nanoparticles and analyze the effect of the particle size and shape on the yield strength. We also compare the absolute and relative strengths of the faceted Pt, Au, and Ni nanoparticles fabricated by similar solid-state dewetting methods.

Materials and methods

We fabricated Pt nanoparticles using a solid-state dewetting method similar to the previously reported fabrication process for Au and Ni nanoparticles [30–32]. We used two different processes to achieve a wide distribution of nanoparticle sizes. Thin Pt films of 10 and 30 nm in thickness were deposited using e-beam evaporation on c-plane-oriented polished (0001) sapphire substrates. The 30-nm-thick film was annealed at the temperature of 1100 °C for 24 h, while the 10-nm-thick film was annealed at 1000 °C for 1 h. Annealing of the 30-nm-thick film resulted in large, relatively symmetrical particles with a wide spread of sizes, while the annealing of the 10-nm-thick film resulted in smaller, asymmetrical, faceted particles with sharp edges. An example of the particles formed as a result of solid-state dewetting of the 30-nm-thick film is shown in Fig. 1. We deformed 75 particles, 48 of them from the 30-nm-thick film featuring an average projected diameter and height of 455 and 240 nm, respectively. The remaining 27 particles were from the 10-nm-thick film, with an average projected diameter and height of 286 and 120 nm, respectively.

We conducted uniaxial compression tests using a Hystrion PI85 PicoIndenter fitted with a flat diamond square punch of $1 \times 1\ \mu m^2$ in size, in displacement control mode with a displacement rate of 1 nm/s. The projected and top facet areas of the particles were determined from micrographs acquired using a Carl Zeiss Ultra Plus high-resolution scanning electron

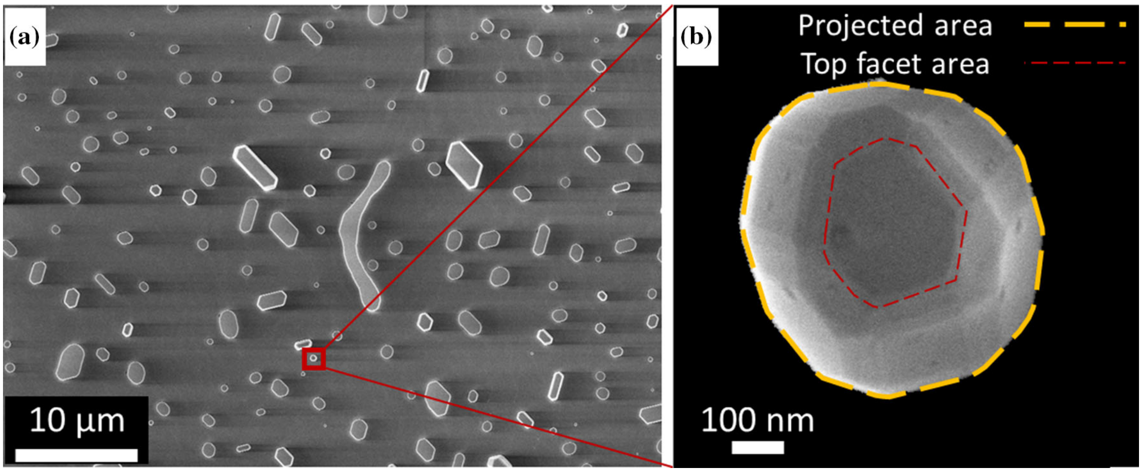

Figure 1 Example of as-fabricated Pt nanoparticles. **a** Large area SEM micrograph of the particles obtained by solid-state dewetting of the 30-nm-thick Pt film at 1100 °C for 24 h. **b** Zoom-in on one of the particles, with projected and top facet areas highlighted. The corresponding diameters were calculated as the square roots of the respective projected/top facet areas.

microscope (SEM). In case of doubt, the pixels at the edge of the SEM image of the upper facet were always assigned to this facet in order to avoid an underestimation of its area, which would have led to an overestimation of the particle strength. The particle height was measured using a XE 70 (Park Systems) atomic force microscope (AFM). Particle facet identification was conducted by calculating normal vectors from high-resolution AFM images. The prevalence of a specific direction among the normal vectors indicated the presence of the corresponding facet orientation. We measured the angles between the identified facets to determine their orientation with respect to each other (details of the method are presented in Supplementary Material). The only prior knowledge about the facet identity we had was the (111) orientation of the top facet parallel to the substrate. The diamond punch was kept nearly perpendicular to the sample surface to ensure homogenous compression. We estimate the maximum misalignment between the punch axis and the substrate normal at 2°. This misalignment minimizes the influence of punch angle on the strength measurements because an average particle with an average elastic displacement at the strain burst would have established a full contact between its upper facet and the punch. We translated the experimentally measured load and displacement values to the engineering stress and strain by normalizing them by the top facet area and the particle height, respectively, measured before the compression test. The engineering stress represents an average compressive stress on the top facet, whereas the local stress distribution is inhomogeneous, with stress concentration at the facet edges and corners [32]. The engineering strain determined in this way overestimates the particle's true compressive strain because the substrate deformation and machine compliance are not taken into account.

Results

Particle compression tests revealed two types of mechanical behavior. Some particles exhibited a catastrophic "strain burst" behavior, in which the particle flattened upon yielding, resulting in a sudden jump of the punch displacement (Fig. 2a). This effect is characteristic of defect-free particles, in which the dislocation nucleation occurs once a critical value of the compressive stress is reached. The strain burst is caused by an avalanche of new dislocations triggered by a nucleation event. The rest of the particles exhibited a "staircase yielding" characterized by small displacement bursts followed by load drops without any dramatic decrease of the particle height. The multiple load drops followed by elasto-plastic loading periods result in a significant decrease of the average slope of the load–displacement curve [36]. This behavior is typical for particles with pre-existing dislocations and dislocation sources. Upon reaching a critical stress, plastic deformation is triggered by the activation of dislocation sources and/or depinning of existing dislocations, causing a displacement burst

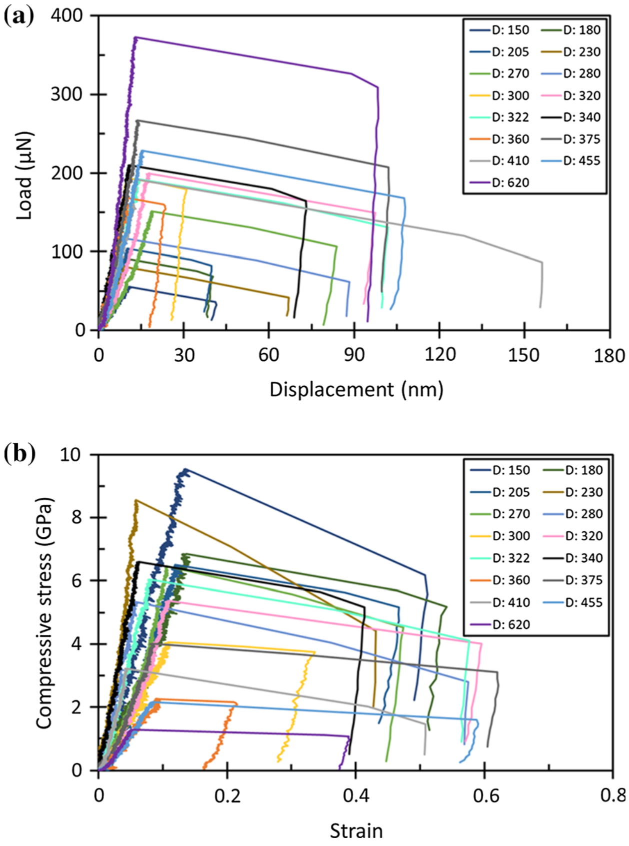

Figure 2 The results of microcompression tests of selected Pt nanoparticles. **a** Load–displacement curves for particles with the upper facet diameters, D_{top}, ranging from 150 to 620 nm, showing that larger particles yield at a higher load. **b** Engineering stress–strain curves of the same particles, demonstrating that the smaller particles yield at a higher stress. The representative particles were randomly selected from the two dewetted samples of 30- and 10-nm-thick Pt films.

followed by the annihilation of dislocations at the particle surface [19, 37, 38]. In what follows, only the particles which failed by a large strain burst will be considered, as only such particles serve our goal of analyzing the nucleation-controlled compressive strength of the nanoparticles. Examples of load–displacement and engineering stress–strain curves for 15 selected particles of different diameters are shown in Fig. 2. The large scatter of slopes in the initial, elastic region of the stress–strain curves in Fig. 2b results from variations in the particle shapes. Due to the large elastic strain at yielding, reaching on average 10%, the shape variations translate into slope variations in the elastic regions of the strain–stress curves. The average stress at strain burst is 4.0 ± 2.1GPa, while for the strongest particles it reaches 9.5 GPa.

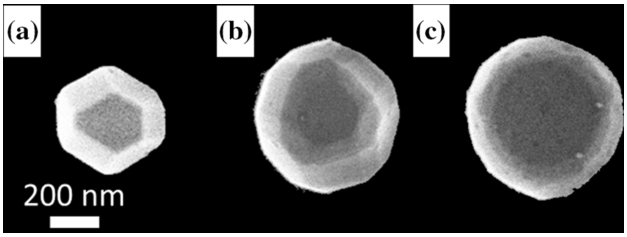

Figure 3 Particles of the three typical shapes. **a** Sharp-edged particle, featuring a small top facet area compared with projected area, with 6 pronounced side facets. **b** Symmetrical particle, featuring a small top facet area compared with the projected area, with more than 6 side facets. **c** Pancake-shaped particle, featuring a large top facet area compared to the projected area, with rounded top facet edges and more than 6 side facets.

Considering the significant variations in the particle shape in the as-fabricated samples, we categorized them into three types, as shown in Fig. 3. Sharp-edged particles (Fig. 3a) feature a large top facet and strongly tilted side facets, similar to the Ni nanoparticles studied by Sharma et al. [31]. Some of these sharp-edged particles exhibit quadruple rather than triple vertices of facets, forming a four- or five-sided top facet instead of the expected six-sided one. Particles of this type were only found in the samples produced from the 10-nm-thick Pt film annealed at 1000 °C for 1 h. The particles from another group exhibited nearly equiaxed shapes (in the projected view), with a small top six-sided facet and more than six side facets (Fig. 3b). Such particles were found mostly in the sample produced by the annealing of the 30-nm-thick Pt film at 1100 °C for 24 h. Lastly, the 'pancake'-shaped particles have a high aspect ratio

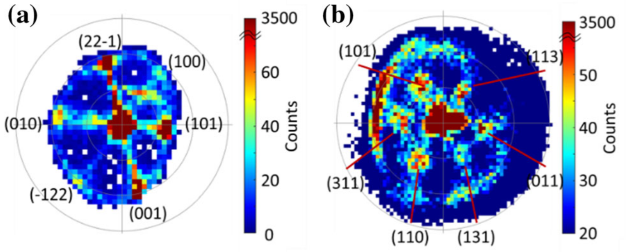

Figure 4 Polar histograms of particle normal directions relative to the [111] normal direction constructed from AFM images. Distance from the center corresponds to θ between 0 and 90°, radial position corresponds to ρ between -180° and 180°. **a** Polar histogram of the sharp-edged particles featuring peaks indicating the prevalence of {100} and {221} type facets; **b** polar histogram of symmetrical particles featuring peaks indicating the prevalence of {110} and {311} type facets.

(Fig. 3c), featuring a relatively low height and a large top facet (of a circular or irregular shape) with rounded edges and without noticeable vertices. Pancake-shaped particles were found in both samples. The nanomechanical testing was performed on 22 pancake, 23 sharp-edged, and 30 symmetrical particles. In Fig. 4, we present a polar histogram of the particle facet orientations produced from AFM data with the aid of a custom code [39], to substantiate our claim that the sharp-edged and symmetrical particles are geometrically different. The facet identification of the chosen sharp-edged particle reveals (100), (101), (001), $(\bar{1}22)$, (010), and $(22\bar{1})$ facet planes (Fig. 4a). The observed higher order {122} and {011} facet planes are different from the facets commonly observed in similar sharp-edged particles of FCC metals exhibiting equilibrium crystal shapes [31]. Some sharp-edged particles exhibit only {001} and {111} facets (Fig. S3 in Supplementary Material), suggesting that their shape can deviate from the equilibrium crystal shape of Pt. In comparison, the symmetrical particles exhibit a larger number of smaller facets (Fig. 3b). The polar histogram for the symmetrical particles (Fig. 4b) reveals that the facets sharing an edge with the top facet are (113), (011), (131), (110), (311), and (101). The higher inclination angle and the smaller facet size make it difficult to identify the steeper facet planes (seen in the polar histogram as smeared arc-shape spots).

Figure 5 shows the particle strength as a function of the projected diameter D_{proj} (square root of the projected area), with the data for the three particle types (sharp-edged, symmetrical and pancake-like) represented by different symbols. Although the shapes of the three particle types differ significantly, the respective strengths completely overlap. Consequently, in what follows, we will analyze the data of all three particle types together. The particle strength follows the power-law behavior $\sigma = AD_{proj}^{-n}$, where A and n ($n \approx 0.96$ being the size exponent) are constants. Figure 5 also shows a change in the slope of the upper envelope of strength at the diameter of about 400 nm.

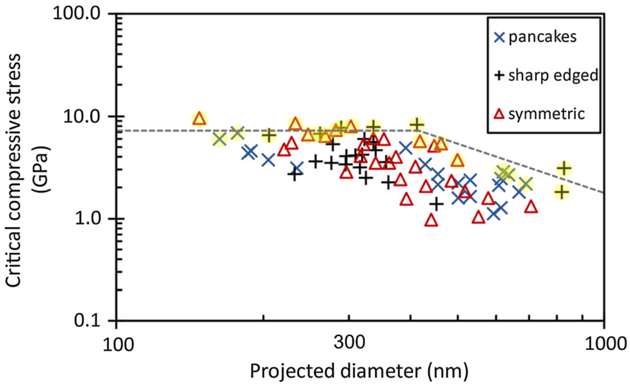

Figure 5 The particle strength as a function of the projected diameter D_{proj}, presented as a double-log plot. Different symbols distinguish the data points for the three particle types. The particle strength σ follows the power law $\sigma = AD_{proj}^{-n}$. The top envelope is marked to highlight the change in slope of maximum strength around $D_{proj} = 400$ nm.

Part of the large scatter of the particle strength in Fig. 5 can be explained by the stochastic nature of the dislocation nucleation process responsible for the onset of yield [26, 40]. Other possible reasons are the inevitable variation in compression parameters between the individual particles and between the two samples, such as a slight misalignment between the top facet and the punch, and the punch surface contamination in the in situ environment of SEM. Yet another important factor is a "hidden" correlation between the particle strength and shape. To reveal this correlation, we introduce the shape parameter $Q = \frac{D_{top}}{D_{proj}}$, where D_{top} and D_{proj} are top facet diameter and the effective diameter of the projected particle area, respectively (Fig. 1). Values of Q close to zero correspond to a spherical or conical shape, while Q values close to 1 are reached by particles of prismatic shape. The plot of Q against D_{proj} (Fig. 6) shows a large spread of the data points, confirming significant variations of particle shapes for the same size. Most Q values are distributed between 0.5 and 0.8,

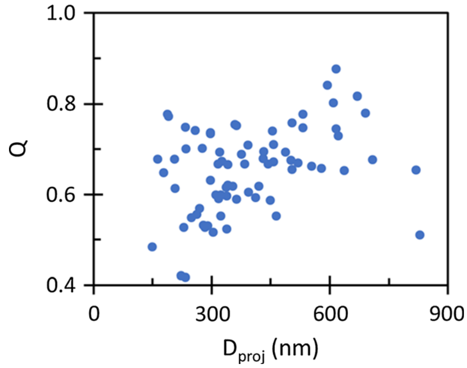

Figure 6 Correlation between the shape parameter Q and the projected diameter of the particles, D_{proj}. Note the large scatter of the particle shapes for the same D_{proj}.

with the pancake-shaped particles exhibiting higher Q and D_{proj} values.

We propose to express the combined size and shape effect on the particle strength in the form of the power law

$$\sigma = BD^{i}_{proj}Q^{j} \quad (1)$$

where B, i, and j are constants. The least-square fit of the data for 75 particles yields $i = -0.74 \pm 0.10$ for the size exponent and $j = -1.66 \pm 0.25$ for the shape exponent (Fig. 7). Strong correlation is observed between the measured strength and the predictions of Eq. (1), with the Pearson correlation factor of 0.812 (Fig. 7a). Another graphical presentation of the power law (1) is obtained by plotting the shape-corrected strength, $^{\sigma}/_{Q^{j}}$ as a function of particle size (Fig. 7b). Compared with the strength-size dependence disregarding the shape effect (Fig. 5), the shape-corrected particle strength exhibits an increasing scatter at high values of D_{proj} while retaining the change in the slope at 400 nm.

Discussion

The shape variations of the particles fabricated in this study were greater than for the previously studied Au and Ni particles [31, 32]. We attribute this shape variability to the metal evaporation during the high-temperature solid-state dewetting annealing of Pt in air. Indeed, already Edison noted that annealing of Pt wires in air results in significant metal loss [41]. This is related to the formation of unstable Pt oxide, which evaporates during annealing. The shape of the Pt particles formed at late stages of dewetting results from an interplay between the capillary effects and the kinetics of evaporation. The evaporation rate sensitively depends on the local airflow in the furnace and the size and shape of the metal islands evolving into particles. Variations in these factors result in a wide dispersion of the final particle shapes. Pt particles annealed in ultra-high vacuum exhibited highly rounded shapes with only {111} and {001} facets present [42], whereas in this study the well-defined {011}, {122}, and {113} facets were also observed (Fig. 4). On the other hand, Au and Ni particles produced by solid-state dewetting exhibited mostly self-similar shapes of the same type [31, 32]. This is because the evaporation did not play any significant role during the dewetting annealing of Ni, and only a minor role during the dewetting of Au [43]. Under these circumstances, the metal islands evolved toward the same shape corresponding to the minimum surface energy for the constant particle volume (equilibrium crystal shape).

In the present study, we only analyzed the particles that yielded in a catastrophic manner with a large displacement burst during compression tests (Fig. 2). This mechanical behavior is typical for defect-free nanostructures. Therefore, our results can be compared with the mechanical behavior of other defect-free metal samples. A natural reference point for the measured compressive strength is the theoretical strength of the respective metals. We assume that the particles yielded by the nucleation of full rather than partial dislocations in the $(111)<110>$ slip system due to the high stacking fault energy of Pt [44]. The shear modulus of Pt in the (111) plane is 54.8 GPa

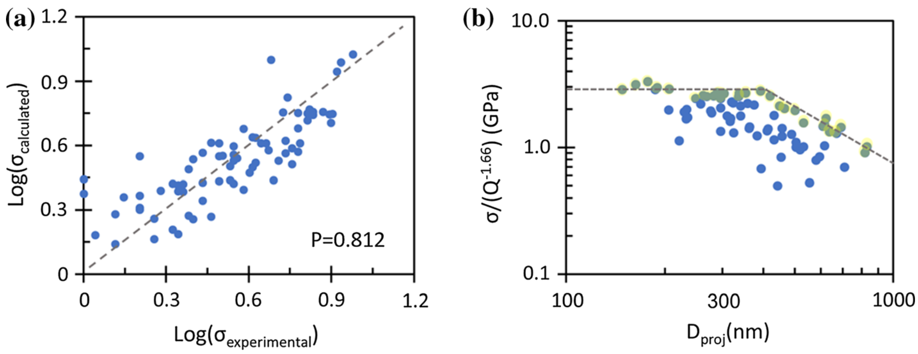

Figure 7 Shape and size dependencies of the particle strength predicted by the power law $\sigma = BD^{i}_{proj}Q^{j}$. **a** Correlation between the experimentally measured strength and predictions of Eq. (1). The Pearson correlation factor P is indicated. **b** Size dependence of strength scaled by the shape parameter. A change of trend in the top envelope (marked in yellow) of the strength is noted at $D_{proj} = 400$ nm.

[45–47], and the critical resolved shear stress (CRSS), τ, of the strongest particle tested here is 2.1 GPa. This value translates to the maximum normalized strength of $G/21$, which is within the $G/2\pi$–$G/30$ limits of the theoretical shear strength. This value is comparable to the maximum shear strength of Ni_3Al nanocubes ($G/17$ [28]) and Mo pillars ($G/26$ [25]). Note that the fabrication methods of the Ni_3Al nanocubes and Mo pillars were different from the one employed in the present study, which makes a direct comparison of the results somewhat problematic. Indeed, Sharma et al. [48] have pointed out that the strength is affected by the surface topography and the defect concentration in the near-surface layer of the sample, which in turn depends on the fabrication method. Therefore, the most direct comparison of our results is with previous compression tests of faceted single-crystalline Au and Ni nanoparticles obtained by the solid-state dewetting technique similar to the one employed in this work. Comparison of the uniaxial strengths of the [111]-oriented Pt, Au, and Ni nanoparticles as a function of their size is shown in Fig. 8a. In Fig. 8b, we compare the normalized CRSS values, also showing the range of the theoretical shear strength according to Polanyi and Frenkel. The smallest particles of all three metals are within the theoretical strength limits, but the Pt nanoparticles are weaker than the Au and Ni particles. They only reach the lower limit of the theoretical strength, while the Ni and Au particles also reach the upper limit (Fig. 8b). This significant difference calls for an explanation.

Density-functional theory (DFT) calculations of the theoretical strength of different FCC metals predict that the τ/G ratio of Ni is twice as high as that of Pt [49]. While this prediction is in qualitative agreement with our results, quantitatively the τ/G values for Ni are nearly a factor of three higher than our experimental values for Pt (Fig. 8b). Sharma et al. [31] suggested that the exceptional strength of Ni nanoparticles may be associated with the presence of a thin native oxide layer covering the particles and impeding the surface nucleation of dislocations. This hypothesis seems to contradict the fact that the Au nanoparticles exhibit the relative strength comparable to that of Ni nanoparticles of similar normalized size (Fig. 8b), while Au oxide is not stable at ambient conditions. We will resolve this contradiction further into the discussion.

Another interesting aspect of the relative strength difference of Pt versus Ni and Au particles is the high stacking fault energy in Pt. However, the high stacking fault energy is expected to make Pt stronger than Au and Ni, which contradicts the experimental observations. Indeed, plastic deformation in the latter two starts with the nucleation of a leading Shockley partial dislocation, as observed in molecular dynamic (MD) simulations [32] of compression of defect-free nanoparticles of low stacking fault energy metals. In Pt, on the other hand, with its relatively high stacking

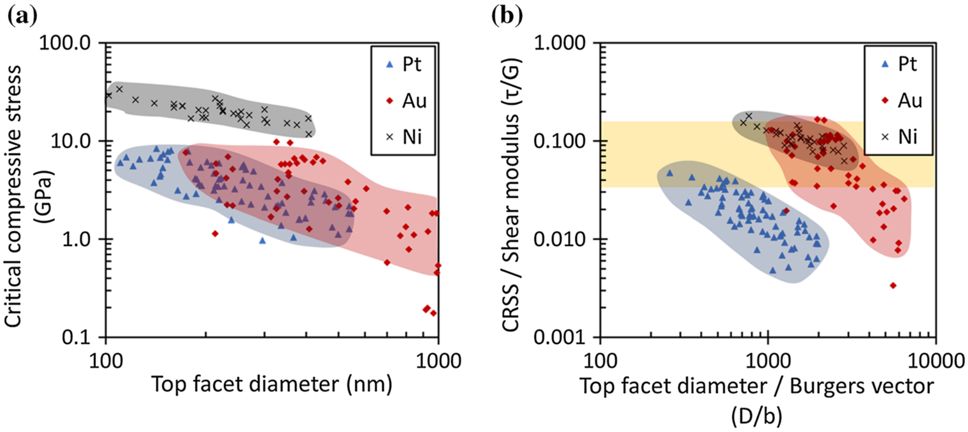

Figure 8 Comparison of the size dependencies of the critical resolved shear strength of Pt (present work), Au [31], and Ni [32] nanoparticles obtained by solid-state dewetting. **a** Critical resolved shear strength as a function of the top facet diameter, demonstrating that Ni particles are significantly stronger than their Au and Pt counterparts exhibiting similar strength. **b** Comparison of the normalized shear strength of Pt, Au, and Ni nanoparticles. The shaded region represents the range of theoretical strength values (from $G/30$ to $G/2\pi$) according to Polanyi and Frenkel. Both Au and Ni nanoparticles approach the upper limit of theoretical strength, while Pt nanoparticles only reach the lower limit.

fault energy, the onset of plasticity is expected to be associated with the nucleation of a full dislocation. The nucleation barrier of this process is expected to be higher than the nucleation barrier for a Shockley partial, resulting in higher strength. This is because the height of the nucleation barrier scales with atomic displacements in the state of the highest energy (transition state), and those scale with the magnitude of the dislocation Burgers vector. Since the Burgers vector of a Shockley partial is smaller than for a full dislocation, a lower nucleation barrier is expected in the former case. Thus, the difference in stacking fault energies cannot explain the difference in strength between the Pt nanoparticles and their Au and Ni counterparts.

We believe that the particle shape plays a leading role in the observed strength anomaly of Pt (compared with Au and Ni). This is suggested by the large scatter of the data points on the strength-size plot in Fig. 5. In the present work, the particle shapes were characterized using two different approaches: either according to qualitative shape features (grouping into three different types of sharp-edged, symmetrical, and pancake-shaped particles) or according to the quantitative shape factor Q. Of the two approaches, only the shape factor seems to correlate with particle strength. The overlap of the datasets representing the three groups of particles in Fig. 5 indicates that the types of the side facets and the sharpness of the edges are not the decisive factors in strength. This is despite the emphasis put on edge curvature by previous studies [31, 32, 48, 50] which presented a positive correlation between edge bluntness and strength. The difference stems from the larger overall shape variation considered in this work, and the focus of previous studies on atomic scale edge sharpness. In this respect, it is worth noting that the edges of the sharp-edged particles studied in the present work are far from being sharp at the atomistic scale, as demonstrated in Fig. S3 in Supplementary Material. On the other hand, we find a strong inverse correlation between the particle strength and the shape factor Q appearing in the power law (1) (see also Fig. 7). Particles with smaller Q values clearly exhibit a higher strength. Since the parameter Q convolutes the wide variety of shape characteristics into a single scalar value, the correlation with strength is not perfect. Nevertheless, the power law (1) allows us to decouple the size and shape effects on the particle strength, at least qualitatively.

In previous studies of mechanical properties of faceted metal nanoparticles, the top facet and projected diameters, D_{top} and D_{proj}, were used interchangeably to describe the size dependence of strength. This could also be done in the present study since D_{proj} and D_{top} correlate (Fig. S4 in Supplementary Material). If the correlation was perfect, then Q would be constant, and the size effect could be represented by either D_{proj} or D_{top}. This was the case in the previous studies [30–32, 48] where the particle shape was close to the self-similar equilibrium Wulff shape. In this case, the power law (1) reproduces the size dependence of strength with the exponent $i = -0.74$. This value is close to the exponents obtained in the earlier reports [30–32, 48]. In the present work, the average value of Q is higher than in the previous studies of equilibrated nanoparticles. This difference can explain the lower strength of the Pt nanoparticles compared with the Au and Ni nanoparticles. Indeed, atomistic simulations [31, 32, 48] suggest that the dislocation nucleation occurs preferentially near the corners and edges of the top facet. Increasing the top facet size (D_{top}) increases the total number of potential nucleation points and thus the probability of a nucleation event. Since, for the same projected size (D_{proj}), particles with larger Q values have a larger top facet, they are likely to fail at a lower compressive stress than particles with smaller Q values. This explains the relative weakness of the Pt particles studied here and the negative sign of the shape exponent j in the power law (1).

Now consider what happens when the size of the top facet D_{top} is fixed, while the projected area diameter D_{proj} is varied. According to Eq. (1), increasing D_{proj} at constant D_{top} increases particle strength (because $|i| < |j|$). The nucleation sites argument cannot explain this increase because the number of nucleation sites is the same for fixed D_{top}. However, increasing D_{proj} at fixed D_{top} means, in most cases, increasing dihedral angle between the top and the side facets. Higher dihedral angle means lower stress concentration at the edges, which means that higher average stress on the top facet is needed to achieve the same level of the local stress at the edge. Thus, for two particles with equal D_{top}, the one with higher value of D_{proj} (and, hence, lower value of Q) will likely fail at higher compressive stress. We would like to emphasize that this conclusion is somewhat counterintuitive. Indeed, increasing D_{proj}

at fixed D_{top} increases the average particle size, and according to previously accepted size effect on strength, this should decrease the particle strength. Yet according to our correlation (1), the strength actually increases.

The analysis based on the parameter Q is consistent with the fact that the normalized strength of Ni_3Al nanocubes [28] and Mo pillars [25] is closer to that of the "weak" Pt particles than to the "strong" Ni and Au particles. The cubes and pillars are characterized by $Q \approx 1$, placing them at the low end of the strength spectrum. On the other hand, the Au particles studied by Mordehai et al. [32] exhibited especially rounded shapes (Q<<1) and thus lay close to the high end of the strength spectrum. The highly faceted Ni particles are closer to the Pt nanoparticles in shape but, as mentioned above, feature a native oxide layer increasing the energy barrier for dislocation nucleation. This solves the apparent contradiction discussed above: while both Au and Ni nanoparticles feature similar normalized strength, it is mainly attributed to small Q values for Au nanoparticles, while the presence of native oxide plays a leading role in their Ni counterparts. Also, the analysis based on the shape parameter Q is consistent with the results of previous studies of Sharma et al. [48] and Kilymis et al. [51] who reported that Wulff-shape nanoparticles of Mo and Si, respectively, are significantly weaker than their spherical counterparts of a similar size. Indeed, the spherical particle can be formally described by a Q factor close to zero, which according to our strength correlation (1) should result in especially high strength (note that the shape exponent j is negative).

Another interesting observation of this work is the change in the slope of the highest strength envelope seen in Fig. 5 and Fig. 7b. For particles smaller than D_{proj} = 400 nm, the slope decreases, hinting at a possible plateau at even smaller sizes. The phenomenon of strength saturation at small sizes was previously reported for Au nanoparticles [30], Mo pillars [25], and Fe nanoparticles [29]. This saturation resolves the paradox that the extrapolation to small sizes exceeds the material's theoretical strength, contrary to the results of atomistic simulations. The strength plateau was previously associated with the theoretical strength of the respective defects-free material [29]. However, the normalized maximum strength of the Au particles is a factor of three higher than that of Mo pillars and Pt particles. This contradiction can be resolved by taking into account the shape dependence of strength. The strength of the Au particles reaches a higher plateau because their shape characterized by small Q values corresponds to a higher strength for the same size. In light of the present work, the plateau strength should be considered as the highest strength achievable in objects of the given shape, and not necessarily the highest strength of the given material.

Finally, the plateau strength of Pt nanoparticles of 7–9 GPa observed in the present work means that Pt nanoparticles of much smaller sizes relevant to catalysis (2–10 nm) also exhibit similar strength, provided the dislocation deformation mechanisms operate at such small sizes. This opens a wide window of opportunities for the strain engineering of their catalytic performance.

Conclusions

The following conclusions can be drawn from the present study:

1. We have fabricated Pt nanoparticles by solid-state dewetting of thin Pt films of two different thicknesses (10 and 30 nm) deposited on a sapphire substrate. The [111]-oriented particles exhibit a large variety of shapes, which we attribute to a competition between the surface energy driving the particle shape toward equilibrium, and the material loss by evaporation during dewetting annealing.
2. Deformation behavior of the Pt nanoparticles in compression has been tested *in situ* inside SEM with the aid of a nanoindentation instrument equipped with a flat diamond punch. Many particles deform elastically up to a large strain of several percent, followed by a single large displacement burst. The rest of the particles deform by a series of small displacement bursts starting at the early stages of the tests.
3. For the particles exhibiting a large displacement burst, the strength follows the "smaller is stronger" trend reported earlier for the faceted Au, Ni, and Mo nanoparticles.
4. We have grouped the particles into three classes according to their general appearance and the number and type of the side facets. No correlation was found between these classes and the

particle strength, indicating that the crystallographic identity of side facets does not have any significant effect on the strength.

5. We have introduced a shape parameter Q characterizing the top facet's size relative to the projected particle size. For the same particle size, the particles with a larger top facet (larger Q) tend to be stronger.
6. The experimental results follow a power law describing the particle strength as a function of its size and shape (Eq. (1)). The size and shape exponents of the strength are generally different.
7. The decrease in the particle strength with an increase in the relative size of the top facet (larger Q) can be explained by the concomitant increase in the total number of dislocation nucleation sites on the top facet. This explanation is consistent with the previous findings indicating that the strength of the pristine Ni_3Al nanocubes and Mo pillars, normalized by the shear modulus, is lower than the strength of faceted nanoparticles, featuring lower Q values.
8. The normalized strength of the Pt particles is a factor of three lower than that of Au and Ni nanoparticles fabricated by the same method. This is consistent with the predictions of DFT calculations of the normalized theoretical shear strength of Pt. We also suggest that part of this effect can be attributed to systematic differences of the particle shapes.

The results of this work clearly indicate that the shape of nanoscale metal specimens can strongly affect their strength. The shape should be considered on par with the specimen size as an important factor in nanoscale plasticity.

Acknowledgements

This work was supported by the Israel Science Foundation, grant No. 617/19. Y. M. acknowledges support from the National Science Foundation, Award No. 1904428.

Data availability

The processed data required to reproduce these findings are available to download from http://dx.doi.org/10.17632/zckcb8strz.1.

Declarations

Conflict of interests The authors declare that they have no conflicts of interests.

Supplementary Information: The online version contains supplementary material available at https://doi.org/10.1007/s10853-021-06435-7.

References

[1] Polsky R, Gill R, Kaganovsky L, Willner I (2006) Nucleic acid-functionalized Pt nanoparticles: catalytic labels for the amplified electrochemical detection of biomolecules. Anal Chem 78:2268–2271. https://doi.org/10.1021/ac0519864

[2] Jianrong C, Yuqing M, Nongyue H et al (2004) Nanotechnology and biosensors. Biotechnol Adv 22:505–518. https://doi.org/10.1016/j.biotechadv.2004.03.004

[3] Conde J, Doria G, Baptista P (2012) Noble metal nanoparticles applications in cancer. J Drug Deliv 2012:1–12. https://doi.org/10.1155/2012/751075

[4] Liang Z, Sun J, Jiang Y et al (2014) Plasmonic enhanced optoelectronic devices. Plasmonics 9:859–866. https://doi.org/10.1007/s11468-014-9682-7

[5] Rodrigues TS, Da Silva AGM, Camargo PHC (2019) Nanocatalysis by noble metal nanoparticles: controlled synthesis for the optimization and understanding of activities. J Mater Chem A 7:5857–5874. https://doi.org/10.1039/c9ta00074g

[6] Ponelyte S, Palevicius A (2014) Novel piezoelectric effect and surface plasmon resonance-based elements for MEMS applications. Sensors (Switzerland) 14:6910–6921. https://doi.org/10.3390/s140406910

[7] Sau TK, Rogach AL (2010) Nonspherical noble metal nanoparticles: colloid-chemical synthesis and morphology control. Adv Mater 22:1781–1804. https://doi.org/10.1002/adma.200901271

[8] Leroy F, Borowik CF et al (2016) How to control solid state dewetting: a short review. Surf Sci Rep 71:391–409. https://doi.org/10.1016/j.surfrep.2016.03.002

[9] Guo D, Xie G, Luo J (2014) Mechanical properties of nanoparticles: basics and applications. J Phys D Appl Phys. https://doi.org/10.1088/0022-3727/47/1/013001

[10] Yu Q, Qi L, Mishra RK et al (2015) Size-dependent mechanical properties of Mg nanoparticles used for hydrogen storage. Appl Phys Lett 106:261903. https://doi.org/10.1063/1.4921003

[11] Pasquini L, Sacchi M, Brighi M et al (2014) Hydride destabilization in core-shell nanoparticles. Int J Hydrog

Energy 39:2115–2123. https://doi.org/10.1016/j.ijhydene.2013.11.085

[12] Khorshidi A, Violet J, Hashemi J, Peterson AA (2018) How strain can break the scaling relations of catalysis. Nat Catal 1:263–268. https://doi.org/10.1038/s41929-018-0054-0

[13] Xia Z, Guo S (2019) Strain engineering of metal-based nanomaterials for energy electrocatalysis. Chem Soc Rev 48:3265–3278. https://doi.org/10.1039/c8cs00846a

[14] Gu XW, Hanson LA, Eisler CN et al (2018) Pseudoelasticity at large strains in Au nanocrystals. Phys Rev Lett 121:56102. https://doi.org/10.1103/PhysRevLett.121.056102

[15] Mordehai D, David O, Kositski R (2018) Nucleation-controlled plasticity of metallic nanowires and nanoparticles. Adv Mater 30:1–17. https://doi.org/10.1002/adma.201706710

[16] Shin J, Chen LY, Sanli UT et al (2019) Controlling dislocation nucleation-mediated plasticity in nanostructures via surface modification. Acta Mater 166:572–586. https://doi.org/10.1016/j.actamat.2018.12.048

[17] Klinger L, Rabkin E (2015) On the nucleation of pores during the nanoscale kirkendall effect. Mater Lett 161:508–510. https://doi.org/10.1016/j.matlet.2015.09.004

[18] Hertzberg RW, Vinc RP, Hertzberg JL (2020) Deformation and fracture mechanics of engineering materials. John Wiley & Sons

[19] Gerard C, Pizzagalli L (2015) Mechanical behaviour of nanoparticles: elasticity and plastic deformation mechanisms. Pramana J Phys 84:1041–1048. https://doi.org/10.1007/s12043-015-0998-4

[20] Greer JR, Nix WD (2006) Nanoscale gold pillars strengthened through dislocation starvation. Phys Rev B Condens Matter Mater Phys 73:1–6. https://doi.org/10.1103/PhysRevB.73.245410

[21] MacMillan NH (1972) The theoretical strength of solids. J Mater Sci 7:239–254. https://doi.org/10.1007/bf00554187

[22] Brenner SS (1956) Tensile strength of whiskers. J Appl Phys 27:1484–1491. https://doi.org/10.1063/1.1722294

[23] Dimiduk DM, Uchic MD, Parthasarathy TA (2005) Size-affected single-slip behavior of pure nickel microcrystals. Acta Mater 53:4065–4077. https://doi.org/10.1016/j.actamat.2005.05.023

[24] Volkert CA, Lilleodden ET (2006) Size effects in the deformation of sub-micron Au columns. Philos Mag 86:5567–5579. https://doi.org/10.1080/14786430600567739

[25] Bei H, Shim S, George EP et al (2007) Compressive strengths of molybdenum alloy micro-pillars prepared using a new technique. Scr Mater 57:397–400. https://doi.org/10.1016/j.scriptamat.2007.05.010

[26] Chen LY, He MR, Shin J et al (2015) Measuring surface dislocation nucleation in defect-scarce nanostructures. Nat Mater 14:707–713. https://doi.org/10.1038/nmat4288

[27] Griesbach C, Jeon SJ, Rojas DF, et al (2021) Origins of size effects in initially dislocation-free single-crystal silver micro- and nanocubes. Acta Mater 214:117020. https://doi.org/10.1016/j.actamat.2021.11702

[28] Maaß R, Meza L, Gan B et al (2012) Ultrahigh strength of dislocation-free Ni_3Al nanocubes. Small 8:1869–1875. https://doi.org/10.1002/smll.201102603

[29] Han WZ, Huang L, Ogata S et al (2015) From "smaller is stronger" to "size-independent strength plateau": towards measuring the ideal strength of iron. Adv Mater 27:3385–3390. https://doi.org/10.1002/adma.201500377

[30] Flanagan TJ, Kovalenko O, Rabkin E, Lee SW (2019) The effect of defects on strength of gold microparticles. Scr Mater 171:83–86. https://doi.org/10.1016/j.scriptamat.2019.06.023

[31] Sharma A, Hickman J, Gazit N et al (2018) Nickel nanoparticles set a new record of strength. Nat Commun 9(1):4102. https://doi.org/10.1038/s41467-018-06575-6

[32] Mordehai D, Lee SW, Backes B et al (2011) Size effect in compression of single-crystal gold microparticles. Acta Mater 59:5202–5215. https://doi.org/10.1016/j.actamat.2011.04.057

[33] Kiener D, Motz C, Rester M et al (2007) FIB damage of Cu and possible consequences for miniaturized mechanical tests. Mater Sci Eng A 459:262–272. https://doi.org/10.1016/j.msea.2007.01.046

[34] Wang H, Xu S, Tsai C et al (2016) Direct and continuous strain control of catalysts with tunable battery electrode materials. Science 354:1031–1036. https://doi.org/10.1126/science.aaf7680

[35] Daio T, Staykov A, Guo L et al (2015) Lattice strain mapping of platinum nanoparticles on carbon and SnO_2 supports. Sci Rep 5:1–10. https://doi.org/10.1038/srep13126

[36] Corcoran S, Colton R, Lilleodden E, Gerberich W (1997) Anomalous plastic deformation at surfaces: nanoindentation of gold single crystals. Phys Rev B Condens Matter Mater Phys 55:R16057–R16060. https://doi.org/10.1103/PhysRevB.55.R16057

[37] Uchic MD, Dimiduk DM, Florando JN, Nix WD (2004) Sample dimensions influence strength and crystal plasticity. Science 305:986–989. https://doi.org/10.1126/science.1098993

[38] Shan ZW, Mishra RK, Syed Asif SA et al (2008) Mechanical annealing and source-limited deformation in submicrometre-diameter nicrystals. Nat Mater 7:115–119. https://doi.org/10.1038/nmat2085

[39] Frederick Zittrell (2021). histogram2Polar (https://github.com/zifredder/histogram2Polar), GitHub. Retrieved 18 August 2021

[40] Bei H, Gao YF, Shim S et al (2008) Strength differences arising from homogeneous versus heterogeneous dislocation nucleation. Phys Rev B Condens Matter Mater Phys 77:060103. https://doi.org/10.1103/PhysRevB.77.060103

[41] Edison TA (1880) Heating metals in vacuo by the electric current. Am J Dent Sci 13:418

[42] Lee WH, Vanloon KR, Petrova V et al (1990) The equilibrium shape and surface energy anisotropy of clean platinum. J Catal 126:658–670. https://doi.org/10.1016/0021-9517(90)90028-I

[43] Malyi O, Rabkin E (2012) The effect of evaporation on size and shape evolution of faceted gold nanoparticles on sapphire. Acta Mater 60:261–268. https://doi.org/10.1016/j.actamat.2011.09.045

[44] Martienssen W, Warlimont H (2006) Springer handbook of condensed matter and materials data. Springer Science & Business Media

[45] Radwan FAA (2012) Isotropy of refractory metals and precious metals. Ijrras 11:37–40

[46] Goldstein RV, Gorodtsov VA, Lisovenko DS (2012) Shear modulus of cubic crystals. Lett Mater 2:21–24. https://doi.org/10.22226/2410-3535-2012-1-21-24

[47] Knowles KM, Howie PR (2015) The directional dependence of elastic stiffness and compliance shear coefficients and shear moduli in cubic materials. J Elast 120:87–108. https://doi.org/10.1007/s10659-014-9506-1

[48] Sharma A, Kositski R, Kovalenko O et al (2020) Giant size- and shape-dependent uniaxial compressive strength of molybdenum nano-and microparticles. Acta Mater 198:72–84. https://doi.org/10.2139/ssrn.3592044

[49] Kamran S, Chen K, Chen L (2009) Ab initio examination of ductility features of fcc metals. Phys Rev B Condens Matter Mater Phys 79:1–8. https://doi.org/10.1103/PhysRevB.79.024106

[50] Amodeo J, Lizoul K (2017) Mechanical properties and dislocation nucleation in nanocrystals with blunt edges. Mater Des 135:223–231. https://doi.org/10.1016/j.matdes.2017.09.009

[51] Kilymis D, Gérard C, Amodeo J et al (2018) Uniaxial compression of silicon nanoparticles: an atomistic study on the shape and size effects. Acta Mater 158:155–166. https://doi.org/10.1016/j.actamat.2018.07.063